ADAPTIVE CONTROL FOR VIBRATION ATTENUATION OF A LASER COMMUNICATION TERMINAL

Frederik Thiele[(1)], **Iñigo Fernandez Imaña**[(2)], **Xavier Manuel Juanpere**[(2)], **Harald Pfifer**[(1)]

[(1)]*Chair of Flight Mechanics and Control, Technische Universität Dresden, 01062 Germany*
{*frederik.thiele, harald.pfifer*}*@tu-dresden.de*
[(2)]*Airbus Defence and Space - 31, Avenue des Cosmonautes - 31402 Toulouse Cedex 4, France*
{*inigo.fernandez-imana, xavier.manuel-juanpere*}*@airbus.com*

ABSTRACT

This paper presents an adaptive control scheme to improve the data transmission rate of a Laser Communication Terminal by attenuating external vibrations. The main contributors for performance degradation are multiple superimposed vibrations originating from the satellite's reaction wheels, which can excite resonance modes. They are introduced to the terminal through its mounting structure and their influence on the pointing error can be modeled as an output disturbance. The proposed controller estimates this disturbance and then attenuates it based on the principle of destructive interference. For that, a combination of internal model control, spectral analysis and modified pseudo-gradient algorithms is used. The developed controller is compared to a high bandwidth H_∞-baseline controller using a nonlinear simulation framework with varying mounting configurations and model uncertainties. To evaluate the performance and robustness of the proposed scheme, a realistic vibration scenario is investigated with multiple parameter studies. The results show a significant improvement of pointing performance over the entire anticipated uncertainty range.

1 INTRODUCTION

Data transmission is a fundamental aspect of every space application, from earth-observation and telecommunication tasks to interplanetary missions. With the steadily increasing number of satellites and the development of more powerful sensors, the amount of data generated in space and the number of communication links rapidly increase. The capabilities of conventional communication methods using radio waves are reaching their limits due to frequency saturation and data transmission rate limitations [13]. Therefore optical communication technology is considered the next evolutionary step for satellite communication applications. It offers a higher transmission bandwidth by at least one order of magnitude, while simultaneously addressing the problem of spectrum exhaustion by using a different electromagnetic frequency spectrum compared to radio communication. The technology is also considered to have a significantly improved security, reduced power consumption and a lower hardware mass [10]. The most common realization for optical communication is a Laser Communication Terminal (LCT). A number of technology demonstrations and commercially used systems are already deployed, e.g. the European Data Relay System (EDRS). The capabilities and current achievements of the EDRS are described in [12], proving its underlying benefits. Moreover, a new generation is already in development with the SkyLight Project to further build on the success of the EDRS [11].

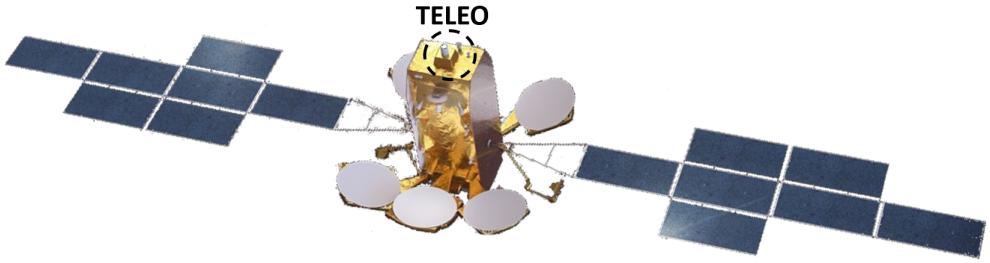

Figure 1: BADR-8 satellite and TELEO laser communication payload built by Airbus Defence and Space

As the communication distance can be several tens of thousands of kilometers and the receiving sensors are only a few centimeters in diameter, improving the pointing performance of the LCT plays a significant role in further enhancing the transmission bandwidth. Several disturbances act on the LCT and deteriorate the pointing performance. The main ones come from the satellite and are transferred to the LCT through its mounting structure. Among those disturbances are micro vibrations from different sources [7]. A preliminary study for a sample satellite identified the vibrations of the reaction wheels as a main contributor to the pointing error, as they can coincide with the resonance frequency of the mounting structure. Typically an array of reaction wheels is used on a satellite. Therefore, the disturbance consists of multiple superimposed vibrations, which can be modeled as a sinusoidal output disturbance. The focus of the presented paper is to reduce the impact of those vibrations on the pointing angle error during data transmission. The setup and requirements are based on the terminal TELEO developed by Airbus, shown in Fig. 1. It is demonstrating the benefits of LCTs for telecommunication applications in flight [14].

Compensation of misalignment is achieved using a Fine Pointing Mechanism (FPM), which is an actuator changing the orientation of a mirror to adjust the laser beam's direction. The proposed adaptive controller estimates the disturbance using internal model control [5] and then calculates an input signal for the FPM to reduce the pointing error using the principle of destructive interference. For that, the frequency, amplitude and phase-offset of each individual sinusoid are determined. The continuous estimation of a frequency is a commonly occurring problem, especially in signal processing tasks. Multiple approaches are described throughout the literature and were investigated for the presented application. Those include spectral analysis [4], phase-locked loops [6], adaptive notch filters [1] and extended Kalman-Filters [3]. For the proposed scheme a spectral analysis using Fast Fourier Transformation (FFT) is identified as the most suitable approach. The amplitude and phase-shift are then determined for each individual frequency with a modification of a pseudo-gradient algorithm (GA) by solving a cost function driven differential equation [8].

The proposed control scheme is applied to a self-standing terminal, i.e., no information about the mounting structure's attitude and reaction wheels' operating conditions are exchanged between satellite and LCT. A mono-dimensional case is presented, which can be easily extended to multi-dimensional applications. At first the investigated LCT setup and control problem is introduced. Then the specific estimation methods for sinusoids are explained, followed by the definition of the entire adaptive control scheme. The approach is then verified using a nonlinear simulation in Matlab/Simulink with a realistic disturbance scenario. The achieved pointing angle error is compared to a high static gain baseline controller by Airbus, which is synthesized using robust optimal H_∞-control techniques.

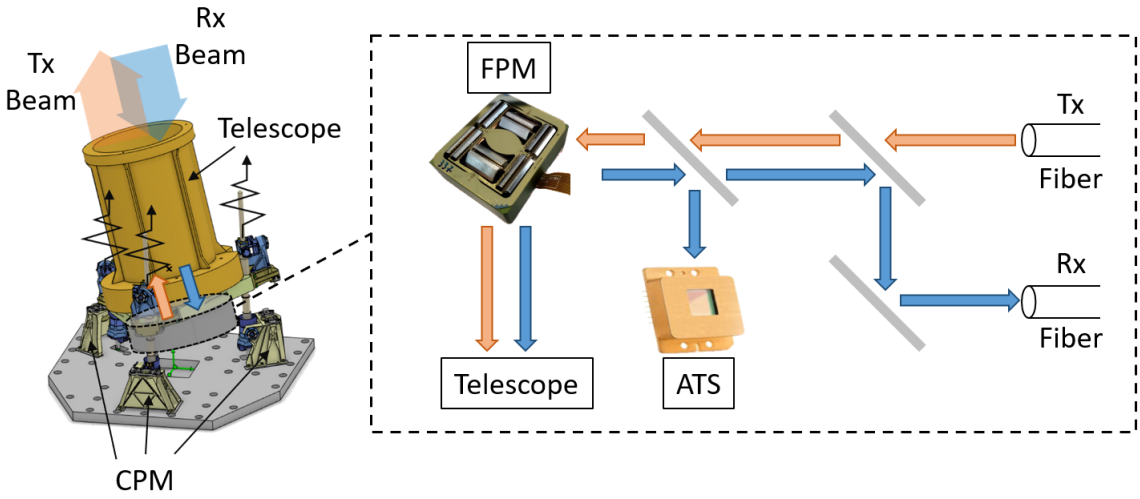

Figure 2: Simplified diagram of pointing, acquisition and tracking sensors and actuators for Laser Communication Terminals, with impact of microvibrations through a Coarse Pointing Mechanism. Thibault Marduel, 2021, Airbus Defence and Space

2 LASER COMMUNICATION TERMINAL

2.1 Assembly and Dynamics

A typical LCT configuration is investigated and a visual schematic representation of the terminal and signal routing is provided in Fig. 2. The focal plane assembly, also referred to as telescope, is modeled as a rigid body. It is comprised of several optical lenses and reflectors to route the reception (Rx) and transmission (Tx) beam through the assembly to their respective fibers. The misalignment between both beams is measured with the Acquisition and Tracking Sensor (ATS), which generates an image from the incoming photons and electrons. The spot position is determined using image processing algorithms and provided as output. The sensor is aligned with the transmission beam, hence only the incoming signal needs to be routed to it. The precise pointing angle adjustments are realized by re-orientating mirrors using the FPM. It can be modeled as a lightly dampened second-order system with the nominal mode frequency and its uncertainty range considered known. The model also contains some uncertainty on the gain magnitude, however its impact is negligible compared to the frequency uncertainty. The entire assembly is connected to the satellite with the Coarse Pointing Mechanism (CPM), which controls the general attitude of the telescope and is also assumed to be a second-order system. Its flexible mode depends on the CPM attitude and thus the exact transfer behavior for a specific point in time is considered unknown.

2.2 Disturbances

The laser communication link requires a high pointing stability and is thus susceptible to various disturbances. The terminal itself introduces measurement and realization errors, while contributors such as thermo-elastics, solar array's rotation, station-keeping transients, star tracker noise and different micro vibrations originate from the satellite. Those are introduced to the terminal through the CPM and are consequently filtered or amplified by the CPM behavior depending on the disturbances' frequency and CPM attitude. Hence, signals within the range of the CPM flexible modes are the main contributors for deteriorating pointing performance. The micro vibrations associated with the reaction wheels' angular rates are identified as the major disturbance contributor within this region.

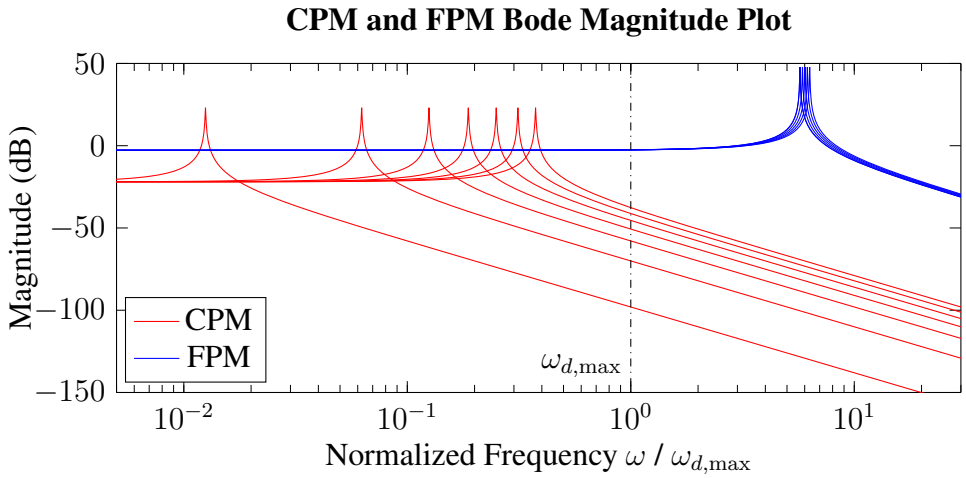

Figure 3: Bode Magnitude Plot showing CPM attitude range and FPM response for different resonance frequencies due to uncertainty

For the investigated satellite a reaction wheel array with four wheels is considered. The corresponding vibration of each wheel can be modeled as a sinusoidal signal $v_{mv,i}$ with $i = 1 \dots 4$ indicating the respective wheel. The vibration's frequency is time-varying, because it depends on the changing angular rate of the wheel. The maximum reachable frequency for the micro vibrations is known and denoted as $\omega_{d,\max}$. The typical evolution for the frequencies over one satellite orbit can be linearly approximated. The initial value and rate of change are different for each wheel due to their orientation. Hence, the frequencies of two vibrations can temporarily coincide. This is referred to as frequency crossing. Additionally the vibrations can excite the CPM flexible mode causing resonance. Both scenarios pose additional challenges and must be taken under consideration for the development of any control scheme.

By design the frequencies of two of those vibrations can be kept out of the critical range. Hence, the disturbance scenarios investigated within this paper considers the combination of just two time-varying vibrations combined into one signal using the principle of superposition as described by

$$v_{mv}(t) = \sum_{i=1}^{2} v_{mv,i}(t). \tag{1}$$

The magnitude of the frequency response of the flexible components are shown in Fig. 3.The frequency is normalized by $\omega_{d,\max}$. Different CPM attitudes are included, covering the entire possible range of transfer behavior. Also the eigenfrequency uncertainty for the FPM is visualized. It is apparent that the resonance frequency range of CPM and FPM are separated. The micro vibrations can coincide with the flexible mode of any CPM attitude but not excite FPM eigenfrequency.

2.3 Operational Modes

Establishing and maintaining an optical communication link between two satellites requires a specific sequence of activities with different operational modes of the LCT. Initially the relative position and velocity of both spacecrafts are assumed unknown. Acquisition is executed with an open-loop scan to find and center the target's beacon by adjusting the telescope's attitude with the CPM. Then a communication link is established and the LCT switches into the transmission mode, during which

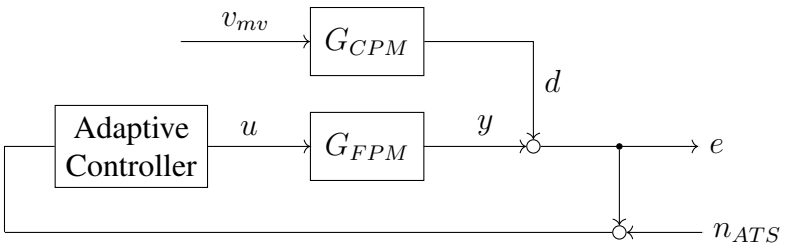

Figure 4: Control problem setup for LCT during data transmission

the FPM operates in closed-loop to maintain the connection and reject disturbances. The CPM holds its position and can be considered quasi-static, only performing FPM desaturation tasks if necessary, i.e., preventing the FPM from reaching its maximum deflection angle by adjusting the CPM's attitude. Within the scope of this paper only the transmission mode is investigated because it imposes the highest constraints for performance and robustness on the system to guarantee a continuous communication link and ensure sufficient data rates. From the operative side, the LCT shall never lose the communication link or exceed the performance specification, neither in steady nor transitory phases, i.e., FPM desaturation. This highly constraints the robustness of the controller, which shall work continuously with no interruption once it is activated. A calibration period at the beginning of the transmission mode during which the requirements are not met is acceptable as long as the link does not get interrupted. Moreover the LCT is supposed to be self-standing, i.e., no information is provided by the satellite such as CPM attitude or reaction wheels' operating conditions.

2.4 Control Problem Definition

In this section the control problem is defined for the investigated scenario described in the previous sections, i.e., the one-dimensional case of a self-standing LCT affected by two superimposed micro vibrations during transmission mode. The quantity of interest and overall output is the pointing angle error e, which indicates the offset between received and transmitted beam. The objective is to minimize e, ideally reaching a zero steady state. The CPM and FPM are second-order linear time-invariant (LTI) systems with the transfer functions G_{CPM} and G_{FPM}, respectively. The FPM takes the control signal u from the adaptive controller and provides the current pointing angle y. The platform accelerations, i.e., the vibrations from Eq. 1, enter the system through the CPM. The resulting projection angle d is modeled as an output disturbance and can be linearly added to the current pointing angle due to small angle assumptions. Hence the pointing angle error is given by

$$e = y + d. \tag{2}$$

The pointing angle error is measured by the ATS while introducing the measurement noise n_{ATS} and then fed back into the adaptive controller closing the loop. Due to the reference value of zero the input to the control is defined as $e + n_{ATS}$. The corresponding block diagram is depicted in Fig. 4.

As described in Sec. 2.3 the CPM attitude and thus its exact transfer function is considered unknown within the control scheme. Based on the forced harmonic response of an LTI system and the fact, that the disturbance acting on the CPM is sinusoidal, the output d can be generally written as

$$d(t) = \sum_{i=1}^{2} d_i(t) = \sum_{i=1}^{2} A_i(t) \sin(\alpha_i(t)) \,, \tag{3}$$

with the time-dependent amplitude $A_i(t)$ and the trigonometric argument

$$\alpha_i(t) = \sigma_i(t) + \Omega_i(t) \tag{4}$$

with

$$\Omega_i(t) = \int_t \omega_i(\tau)\mathrm{d}\tau. \tag{5}$$

The changing frequency of a vibration is accounted for by $\omega_i(t)$ and the resulting time-varying phase-offset due to the CPM transfer is denoted as $\sigma_i(t) \in [0, 2\pi]$. An analytical description of the latter quantity is not available, because the CPM transfer is considered unknown and quasi-steady. However its exact value is also not needed as will become apparent later when the adaptive scheme is described in detail.

3 BACKGROUND

3.1 Frequency Estimation

Frequency estimation of an unknown and/or time-varying frequency is a commonly occurring problem within control and signal processing applications. Within the presented paper the estimation of the disturbance frequencies, i.e., the micro vibration frequencies, encompasses some unique challenges. The employed method needs to be robust regarding initial conditions, CPM resonance cases and frequency crossing. For the listed requirements an estimation scheme using spectral analysis, more specifically FFT, is identified as the most suitable approach. However a standard FFT requires a time-fixed vector of the signal to be analyzed, but a time-continuous frequency estimation is needed for the investigated control problem. An approach similar to an adaptive frequency-domain filter described in [2] is implemented.

Assume an arbitrary continuous signal $x(t) \in \mathbb{R}$ and a buffer vector $X(t) \in \mathbb{R}^L$ providing a continuously updated time-series of $x(t)$ measured by a sensor with a known sampling frequency f_s. The vector follows the *first-in-first-out* principle and is defined as

$$X(t) = \begin{bmatrix} x\Big(t - (L-1)\Delta t_s\Big) & \cdots & x(t - 2\Delta t_s) & x(t - \Delta t_s) & x(t) \end{bmatrix}^{\mathrm{T}}, \tag{6}$$

with the sampling rate $\Delta t_s = f_s^{-1}$ and the number of measurements L. The sampling frequency needs to be above the Nyquist frequency of the highest expected frequency of interest. An online frequency estimation is then obtained by repeatedly performing an FFT with the frequency f_{FFT} for the current buffer vector. An additional post-processing step after the FFT is introduced, which determines the frequency corresponding to the largest magnitude within the spectrum. Note that the frequency f_{FFT} can differentiate from the sampling frequency f_s, with an integer multiple being the most reasonable choice.

The estimation accuracy of the FFT depends directly on the frequency resolution

$$\Delta f = \frac{f_s}{L}, \tag{7}$$

which is the smallest detectable frequency difference. Moreover, for a dominant signal with differentiable time-varying frequency, the estimated value corresponds to the average frequency over the time period included in the buffer vector, i.e., $L\,\Delta t$. Therefore the estimation becomes more precise for smaller L. Note that the vector length L can not be decreased indefinitely for the FFT to work properly. A accuracy trade-off for different buffer dimensions is apparent.

For easier notation during the control design the operator $Freq(\cdot)$ is defined, which provides an online estimation of the most dominant frequency in a continuous signal. It combines the previously

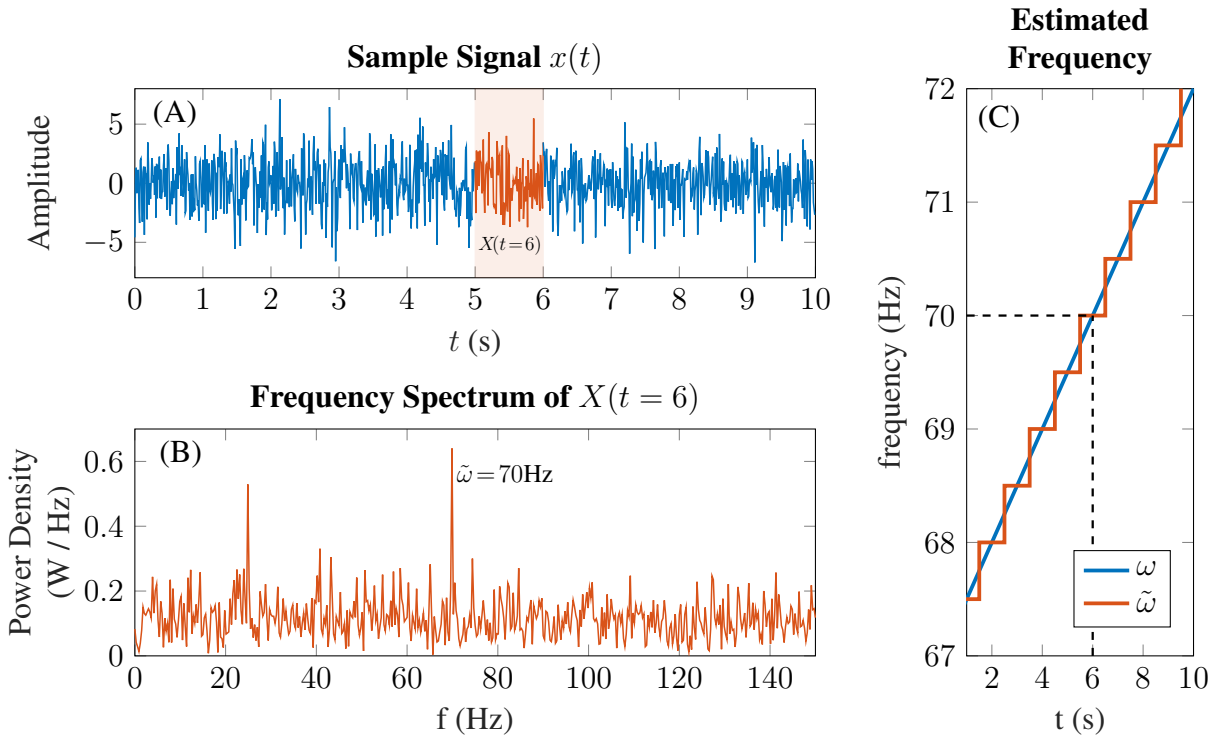

Figure 5: Process of frequency estimation for an arbitrary signal

described steps of updating the buffer vector and executing the FFT and post-processing steps. Moreover the operator provides the latest estimated value until it is updated to obtain a continuous signal. In Fig. 5 the described process is visualized for a sample signal containing two sinusoids with time-dependent frequency and superimposed white noise. Subplot (A) shows the signal $x(t)$ and highlights the buffer vector $X(t=6)$. The spectral analysis of the vector is displayed in the subplot (B) with the estimated frequency $\tilde{\omega}$. The time-dependent frequency $\omega(t)$ and its estimation $\tilde{\omega}(t)$ of the dominant sinusoid in $x(t)$ are shown in Subplot (C).

Due to the described properties and restriction, the provided frequency estimation shows a characteristic stair-function behavior in a continuous simulation as shown in Fig. 5. The step-height depends on the frequency resolution, while the step-width is influenced by f_s, f_{FFT} and L. This concludes that the accuracy of the frequency estimation is directly dependent on the available hardware.

3.2 Modified Pseudo-Gradient Algorithm

Assume a signal d containing two arbitrary superimposed sinusoids as in Eq. 3 with $\Omega_1(t)$ and $\Omega_2(t)$ in Eq. 5 considered known for all t. An adaptive algorithm is employed to determine one of those sinusoids d_i and remove it from the input signal. This is achieved by adapting the parameter of an internal comparison signal of the form

$$c_i(t) = \theta_{c,i}(t)\cos\big(\Omega_i(t)\big) - \theta_{s,i}(t)\sin\big(\Omega_i(t)\big), \tag{8}$$

with the adaptive parameters $\theta_{c,i}$ and $\theta_{c,i}$ to match the original sinusoid for a specific $\Omega_i(t)$. The algorithm converges to

$$\lim_{t\to\infty} c_i(t) \approx d_i(t). \tag{9}$$

The structure presented in Eq. 8 is appropriate for sinusoidal signals due to its capability to reflect any amplitude or phase-offset, as can be shown using angle sum identities. This implies that the adaptive

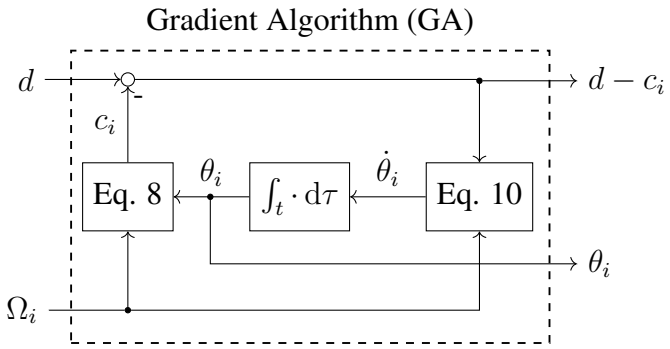

Figure 6: Schematic of modified pseudo-gradient algorithm

parameter can also account for any possible value of $\sigma_i(t)$ in Eq. 4. Therefore no exact knowledge of this phase-offset is needed for the presented approach, as stated in Sec. 2.4.

The update law for the adaptive parameter is defined to minimize a cost function with the established least-mean-square method described in [5]. The cost function selection is based on the work of [9], where a similar approach is used to attenuate periodic disturbances. The update law is given by the differential equation

$$\begin{bmatrix} \dot{\theta}_{c,i}(t) \\ \dot{\theta}_{s,i}(t) \end{bmatrix} = g\big(d(t) - c_i(t)\big) \begin{bmatrix} \cos\big(\Omega_i(t)\big) \\ -\sin\big(\Omega_i(t)\big) \end{bmatrix}, \tag{10}$$

with the cost function $d(t) - c_i(t)$ and the adaptive gain g. Higher gains improve the capability to react to rapid changes of the original signal, e.g., increasing amplitude during CPM resonance. However, they can also cause the algorithm to become unstable [9]. Introducing an internal feedback by including the adapted signal c_i in the cost function increases the overall stability of the algorithm. This allows large enough g for satisfactory performance during critical situation, e.g., CPM resonance, without causing instability. The initial values for the parameters and their derivatives are set to

$$\theta_{c,i} = \theta_{s,i} = \dot{\theta}_{c,i} = \dot{\theta}_{s,i} = 0. \tag{11}$$

A schematic representation of the described method in a converged state is provided in Fig. 6 with the vectors $\theta_i = [\theta_{c,i}, \theta_{s,i}]^T$ and $\dot{\theta}_i = [\dot{\theta}_{c,i}, \dot{\theta}_{s,i}]^T$.

4 ADAPTIVE CONTROLLER

In this section, the entire adaptive control scheme is presented which is depicted in Fig. 7. It is comprised of an internal model control scheme to estimate the disturbance, the determination of its individual sinusoidal components and the construction of the FPM's input signal. Each aspect is described in detail in their respective subsections. In addition, a second-order low-pass filter is implemented in front of the FPM to attenuate sensor noise and prevent exciting the FPM flexible mode through resonance within the loop. Its roll-off frequency is chosen to not interfere with other components of the adaptive scheme.

Note that various quantities are estimated throughout the scheme, which are then denoted with a tilde. Also the notation for quantities in the time and frequency domain is identical. The distinction can be inferred by context.

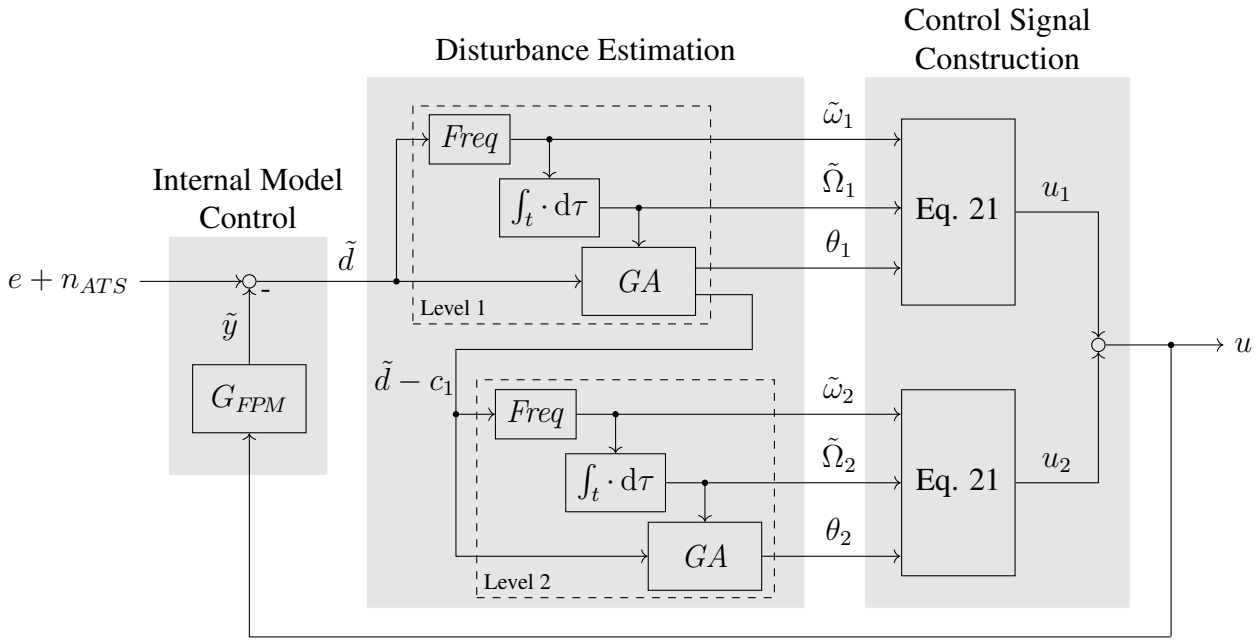

Figure 7: Structure of adaptive controller

4.1 Internal Model Control

The signal d, introduced as an output disturbance to the control loop, is estimated in its entirety using an internal model control structure. The input to the scheme is the measured pointing angle error $e + n_{ATS}$ and the control signal u. An estimation of the current pointing angle $\tilde{y}$ is obtained using the transfer function for the nominal FPM plant and can be written as

$$\tilde{y} = G_{FPM}\, u = y + \Delta y. \tag{12}$$

The difference Δy to the exact value y is the result of FPM model uncertainties. However, the proposed scheme provides sufficient robustness for the expected eigenfrequency uncertainties of the FPM. Thus it is assumed, that

$$\Delta y \approx 0 \rightarrow \tilde{y} \approx y. \tag{13}$$

The estimated FPM output is then subtracted from the measured signal. Using Eq. 2 and Eq.13 the estimated disturbance including measurement noise can be written as

$$\tilde{d} = e + n_{ATS} - G_{FPM}\, u = d + y + n_{ATS} - \tilde{y} = d + n_{ATS}. \tag{14}$$

It is assumed that the content of the measurement noise at the disturbance frequency is negligible compared to the disturbance itself. Therefore, it does not negatively impact the subsequent steps of the adaptive controller.

4.2 Disturbance Estimation

In this step, the individual components making up the signal $\tilde{d}$ are estimated and parameterized. The proposed approach is tailored specifically to the expected harmonic signals caused by the micro vibrations using the methods introduced in Sec. 3. The estimation of the individual signal components $\tilde{d}_i$ is implemented in a cascade setup, which provides robust behavior during frequency crossing. Without loss of generality the order of the signal components in $\tilde{d}$ coincides with their corresponding amplitude, i.e., $\tilde{d}_1$ has the largest and $\tilde{d}_2$ the second largest.

Each cascade level consists of multiple steps. At first, the frequency $\tilde{\omega}_i$ is estimated. Then, the trigonometric argument $\tilde{\Omega}_i$ is calculated analog to Eq. 5. Afterwards, the modified pseudo-gradient algorithm is applied. The update law Eq. 10 is defined in a general form for each level by

$$\begin{bmatrix} \dot{\theta}_{c,i}(t) \\ \dot{\theta}_{s,i}(t) \end{bmatrix} = g \begin{bmatrix} \cos\left(\tilde{\Omega}_i(t)\right) \\ -\sin\left(\tilde{\Omega}_i(t)\right) \end{bmatrix} \sum_{k=0}^{i} -c_k(t), \tag{15}$$

with $c_0(t) = -\tilde{d}(t)$. The internal comparison signal Eq. 8 can be rewritten as

$$c_i(t) = \theta_{c,i}(t) \cos\left(\tilde{\Omega}_i(t)\right) - \theta_{s,i}(t) \sin\left(\tilde{\Omega}_i(t)\right) \tag{16}$$

to correctly indicate the estimated frequency. In a last step, the output signal of the gradient algorithm is provided to the next cascade level.

4.3 Control Signal Construction

The control signal is designed so that the FPM output attenuates the disturbance d in Fig. 4

$$G_{FPM}\, u = y \approx -d \;\rightarrow\; e \approx 0 \tag{17}$$

using the principle of destructive interference. It is composed of multiple superimposed harmonic signals and can be written as

$$u = \sum_{i=1}^{2} u_i \tag{18}$$

to address each vibration separately. The individual signals u_i are based on the internal signal c_i of the modified pseudo-gradient algorithm in Eq. 16 but with adjusted amplitude and phase.

The nominal FPM response to sinusoidal input is evaluated at specific frequencies, i.e., the estimated disturbance frequencies. Based on the forced harmonic response the following notations are introduced for the system gain

$$|G_{FPM}(j\omega)| = \sqrt{\mathrm{Re}^2\left(G_{FPM}(j\omega)\right) + \mathrm{Im}^2(G_{FPM}(j\omega))} \tag{19}$$

and phase-shift

$$\varphi_{FPM}(\omega) = \arctan\left(\frac{\mathrm{Im}(G_{FPM}(j\omega))}{\mathrm{Re}(G_{FPM}(j\omega))}\right). \tag{20}$$

Each signal u_i is adjusted by the inverse FPM behavior at the corresponding frequency $\tilde{\omega}_i$, i.e., divided by the gain and adjusted for the negative phase-shift. An additional phase-shift by π is introduced to each sinusoid effectively inverting the sign. This is necessary to attenuate the disturbance instead of amplifying it. The individual control signals are defined by

$$u_i = |G_{FPM}(j\tilde{\omega}_i)|^{-1} \Big[\theta_{c,i} \cos\left(X_i\right) - \theta_{s,i} \sin\left(X_i\right)\Big], \tag{21}$$

with the trigonometric argument

$$X_i = \tilde{\Omega}_i - \varphi_{FPM}(\tilde{\omega}_i) - \pi. \tag{22}$$

Note that the time dependency is omitted for improved readability in Eq. 21 and Eq. 22.

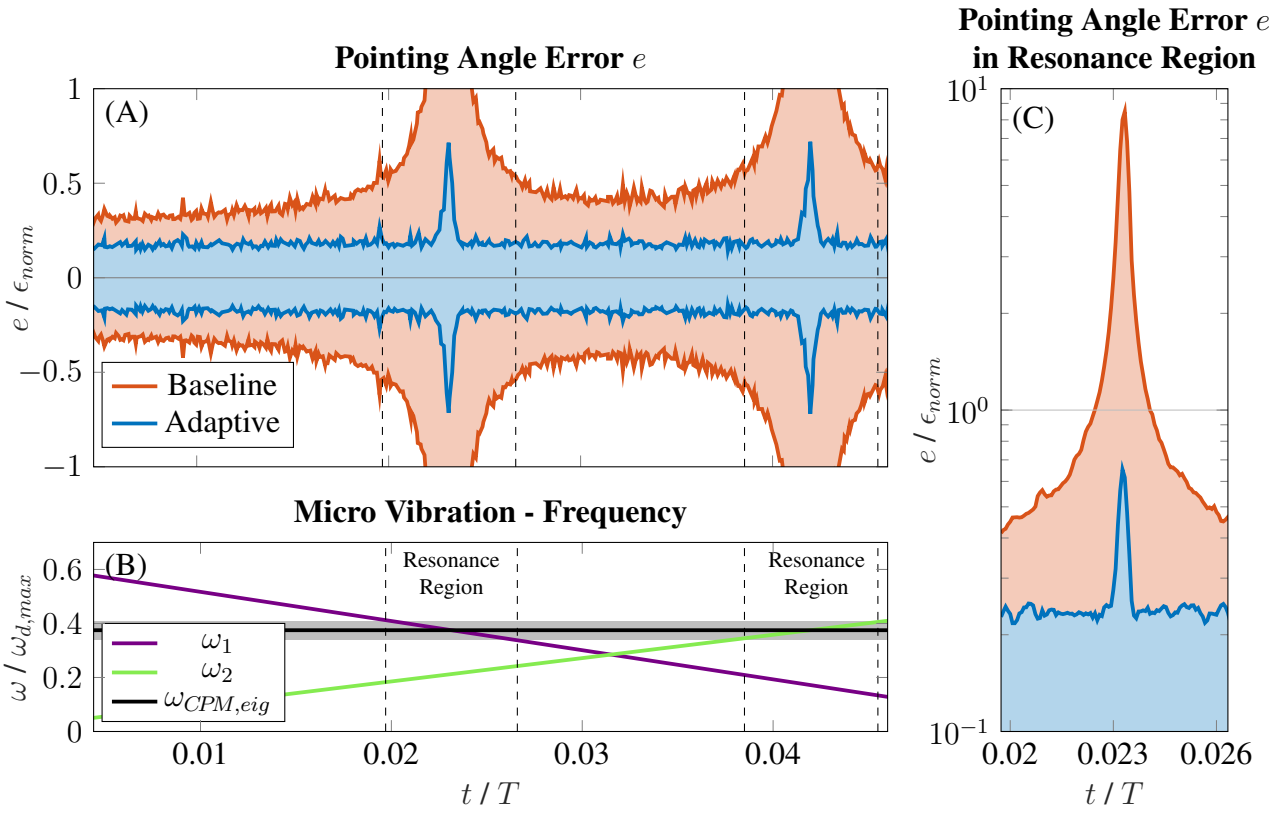

Figure 8: Pointing angle error for a section of a realistic vibration scenario

5 NONLINEAR SIMULATION RESULTS

The developed control scheme is investigated with a nonlinear Simulink simulation in Matlab. A realistic disturbance scenario is implemented to compare the achieved pointing performance of the proposed scheme with a state-of-the-art baseline controller. The exact values for the vibration scenario, sensor noise, and pointing requirements as well as the baseline controller are provided by Airbus.

The scenario consists of two vibrations and covers one orbital period T which is several hours long. However, for improved visualization of the results only a section of a few dozen minutes is shown. The pointing performance in that section is representative for the complete scenario. Additionally the entire CPM attitude range was investigated, but only the results for the worst-case configuration are depicted. The time-dependent frequency of each vibration is given by a continuous piece-wise linear function. It is depicted in Subplot B of Fig. 8 together with the CPM eigenfrequency denoted by $\omega_{CPM,eig}$. The values are normalized with the maximum disturbance frequency and the time axis is normalized with the orbital period T. The disturbances are further given by a frequency-dependent amplitude, initial frequency value and phase-offset.

The pointing angle error requirement ϵ_{norm}, which is a few micro radians, is provided to guarantee the desired data transmission rate. A secondary requirement $\epsilon_{res} \approx 10\,\epsilon_{norm}$ is given for the CPM resonance case, which ensures that the communication link is not interrupted. The potential reduction in data transmission rate is considered acceptable, because the resonance regions only make out a fraction of the entire scenario. A resonance region occurs if the frequency of one vibration is within the margin $\Delta\omega_{res}$ around the CPM flexible mode. The corresponding regions are label in Subplot B

of Fig. 8 and the margin is indicated by the gray zone around $\omega_{CPM,eig}$. The overall requirement is described by

$$\epsilon(\omega) = \begin{cases} \epsilon_{res} & |\omega_{CPM,eig} - \omega_i| \leq \Delta\omega_{res} \\ \epsilon_{norm} & \text{otherwise.} \end{cases} \tag{23}$$

Subplot A of Fig. 8 shows the pointing angle error e of the proposed adaptive scheme versus the baseline controller. It is normalized by the requirement ϵ_{norm}. The error is generally a zero-mean sinusoid. For improved visibility the upper and lower contours of the signal are highlighted. During normal operation, i.e, outside of resonance regions, the adaptive controller performs on average approximately 38% better than the baseline controller. An even more significant improvement is observable in the resonance regions, during which the baseline controller is only able to meet the secondary pointing requirement. Therefore, the absolute value of the pointing angle error is depicted on a logarithmic scale in Subplot C of Fig. 8. The achieved error with the adaptive scheme is more then one order of magnitude smaller and still meets the requirement given for normal operation.

The chosen scenario section includes two additional interesting aspects to evaluate the adaptive scheme. Firstly, the frequency crossing occurring at around $0.031t/T$. Secondly, the dominant disturbance component, i.e., the vibration with the largest amplitude, changing between both resonance regions. This can be inferred by both vibrations causing CPM resonance at some point during the scenario. Moreover, the robustness of the scheme towards FPM uncertainties was investigated using Monte Carlo Simulations. No noticeable impact on the performance can be observed for either situation. This shows, that the selected cascade setup is a appropriate scheme capable to scope with multiple vibrations, rapidly changing amplitudes during CPM resonance and the instantaneous switch between tracked signals of each level.

6 CONCLUSION

An adaptive scheme to improve pointing performance of an LCT is presented. The most dominant disturbances are identified as micro vibrations created by the reaction wheels of the satellite. They act as an output disturbance on the LCT control loop. Nonlinear simulations are used to verify the scheme and evaluate its performance. Comparison with a baseline controller shows significant improvements, especially during structural resonance cases. This concludes that the presented adaptive controller is highly effective in attenuating sinusoidal output disturbances. With vibrations being a major source for pointing angle errors this paper provides a valuable contribution to further improve the capabilities in the space industry.

ACKNOWLEDGMENT

The presented work was developed in cooperation between the Technische Universität Dresden and Airbus Defence and Space as part of the ESA-funded project No. AO/111017/21/NL/MGu entitled Adaptable Control and Estimation with Guaranteed Robust Performance (ACE).

REFERENCES

[1] P. Regalia, “An improved lattice-based adaptive iir notch filter”, *IEEE Transactions on Signal Processing*, vol. 39, no. 9, pp. 2124–2128, 1991.

[2] D. R. Kuo Sen M; Morgan, *Active Noise Control Systems, Algorithms and DSP Implementations*. Wiley Series, 1996.

[3] S. Bittanti and S. Savaresi, “On the parametrization and design of an extended kalman filter frequency tracker”, *IEEE Transactions on Automatic Control*, vol. 45, no. 9, pp. 1718–1724, 2000.

[4] T. Tsuei, A. Srinivasa, and S. Kuo, “An adaptive feedback active noise control system”, *IEEE International Conference on Control Applications*, pp. 249–254, 2000.

[5] S. J. Elliott, *Signal Processing for Active Control*. Academic Press, 2001.

[6] B. Wu and M. Bodson, “A magnitude/phase locked-loop approach to parameter estimation of periodic signals”, *American Control Conference*, vol. 5, pp. 3594–3599, 2001.

[7] T. Jono, M. Toyoshima, N. Takahashi, T. Yamawaki, K. Nakagawa, and A. Yamamoto, “Laser tracking test under satellite microvibrational disturbances by oicets atp system”, *Acquisition, Tracking, and Pointing XVI*, vol. 4714, pp. 97–104, 2002.

[8] B. Wu and M. Bodson, “Multi-channel active noise control for periodic sources - indirect approach”, *Automatica*, vol. 40, no. 2, pp. 203–212, 2004.

[9] M. Bodson, “Rejection of periodic disturbance of unknown and time-varying frequency”, *International Journal of Adaptive Control and Signal Processing*, vol. 19, pp. 67–88, 2005.

[10] M. Gregory, F. Heine, H. Kämpfner, R. Meyer, R. Fields, and C. Lunde, “Tesat laser communication terminal performance results on 5.6gbit coherent inter satellite and satellite to ground links”, *International Conference on Space Optics*, 2010.

[11] H. Hauschildt, C. Elia, H. L. Moeller, and D. Schmitt, “Scylight — esa’s secure and laser communication technology framework for satcom”, *IEEE International Conference on Space Optical Systems and Applications*, pp. 250–254, 2017.

[12] H. Hauschildt, N. le Gallou, S. Mezzasoma, *et al.*, “Global quasi-real-time-services back to Europe: EDRS Global”, *International Conference on Space Optics*, 2018.

[13] M. Toyoshima, “Recent trends in space laser communications for small satellites and constellations”, *Journal of Lightwave Technology*, vol. 39, no. 3, pp. 693–699, 2021.

[14] P. Berceau, S. Angibault, A. Barbet, *et al.*, “Space optical instrument for geo-ground laser communications”, *International Conference on Space Optics*, 2022.